RESEARCH ARTICLE

Transient Superdiffusion of Energetic Carriers in Transition Metal Dichalcogenides Visualized by Ultrafast Pump-Probe Microscopy

Yun-Ke Zhou, Xiao-Ze Li, Qian-Ni Zhou, Ren-Hao Xing, Yan Zhang, Benfeng Bai[*], **Hong-Hua Fang**[*], **and Hong-Bo Sun**

State Key Laboratory of Precision Measurement Technology and Instruments, Department of Precision Instrument, Tsinghua University, Beijing 100084, P. R. China.

*Address correspondence to: hfang@mail.tsinghua.edu.cn (H.-H.F.); baibenfeng@mail.tsinghua.edu.cn (B.B.)

Because of the strong Coulomb interaction and quantum confinement effect, 2-dimensional transition metal dichalcogenides possess a stable excitonic population. To realize excitonic device applications, such as excitonic circuits, switches, and transistors, it is of paramount importance for understanding the optical properties of transition metal dichalcogenides. Furthermore, the strong quantum confinement in 2-dimensional space introduces exotic properties, such as enhanced phonon bottlenecking effect, many-body interaction of excitons, and ultrafast nonequilibrium exciton–exciton annihilation. Exciton diffusion is the primary energy dissipation process and a working horse in excitonic devices. In this work, we investigated time-resolved exciton propagation in monolayer semiconductors of WSe_2, $MoWSe_2$, and $MoSe_2$, with a home-built femtosecond pump-probe microscope. We observed ultrafast exciton expansion behavior with an equivalent diffusivity of up to 502 cm^2 s^{-1} at the initial delay time, followed by a slow linear diffusive regime (20.9 cm^2 s^{-1}) in the monolayer WSe_2. The fast expansion behavior is attributed to energetic carrier-dominated superdiffusive behavior. We found that in the monolayers $MoWSe_2$ and $MoSe_2$, the energetic carrier-induced exciton expansion is much more effective, with diffusivity up to 668 and 2295 cm^2 s^{-1}, respectively. However, the "cold" exciton transport is trap limited in $MoWSe_2$ and $MoSe_2$, leading to negative diffusion behavior at later time. Our findings are helpful to better understand the ultrafast nonlinear diffusive behavior in strongly quantum-confined systems. It may be harnessed to break the limit of conventional slow diffusion of excitons for advancing more efficient and ultrafast optoelectronic devices.

Introduction

In the past few years, 2-dimensional (2D) transition metal dichalcogenides (TMDs) have emerged as a highly promising class of functional materials for next-generation optoelectronics [1–5], such as field-effect transistors [2], solar cells [3], light-emitting diodes [4], and laser modulators [5]. This is largely due to their prominent optoelectronic properties, for example, direct bandgap [6,7], valley selective optical coupling [8,9], extremely large binding energies of excitons [10,11], and strong nonlinear optical response [12,13]. Excitons, which are stable in TMDs at room temperature [14,15], dominate the optical properties in TMD and the performance of the TMD-based devices [16,17]. In this context, it is essential to investigate the exciton movement in 2D TMDs. This has substantial implications, including exciton manipulation for quantum photonic technologies [18–20], as well as addressing the interplay between many-body interaction and propagation [21,22]. Moreover, to realize 2D material-based excitonic devices [9,23–26] such as excitonic circuits, switches, transistors, and transducers, understanding and controlling their spatial degree of freedom is one of the crucial considerations. However, knowledge on exciton transport in 2D materials is limited.

Generally, excitons will transport from high concentration region to low concentration region driven by the population gradient. This phenomenon is known as exciton diffusion. The classical exciton diffusion is a linear process [27–29] as described by the diffusion equation. Recent experimental investigations have shown several nonclassical exciton transport behaviors in 2D materials. For instance, Kulig et al. [30] reported the halo effect in monolayer WS_2, where the initial Gaussian distribution of the exciton population evolves into long-lived halo shapes at high injected exciton densities. Considering the spatial temperature gradient due to the emission and reabsorption of hot optical phonon, this phenomenon can be explained by introducing thermal drift into the diffusion equation [31]. In addition, there is another nonlinear, anomalous diffusion behavior called subdiffusion [14], presenting an initial normal diffusion followed by a slower subdiffusive regime. The time-varying diffusion coefficient was attributed to the disorder in the strained monolayer WSe_2 system. Deviating from the above anomalous diffusion behaviors, superdiffusion [32] occurs on ultrafast time scales, and its effective diffusivity coefficient can reach up to hundreds of square centimeters per second. Therefore, superdiffusion can decrease carrier loss by improving spatial migration as it is a scatter-free process, thus breaking the

efficiency limitation of optoelectronic devices such as solar cells. In addition, the characteristics of ultrashort time scales [33] make superdiffusion promising to be applied to petahertz opto-electronic devices such as ultrahigh-speed photodetectors. Such superior diffusive behavior has been examined in silicon [34], organic semiconductors [35], perovskite [36,37], and metallic gold [38,39]. More recently, the hot carrier expansion in multilayer WS_2 has been reported by Liu et al. [32]. These researches indicate that ultrafast nonequilibrium effects and many-particle scattering processes play an essential role in the spatial propagation of exciton in 2D materials, motivating the necessity to investigate ultrafast exciton diffusion and its interplay with many-particle scattering processes. Isoelectronic 2D TMD alloys exhibit tunable electrical and optical properties due to the modulation of their band structure and carrier mobility [40,41], which may affect the exciton transport process simultaneously. In addition, the defect or dielectronic disorder may also play an important role in transport dynamics. Thus, a comprehensive understanding of the function of metal atomic substitution on the ultrafast exciton diffusion in 2D materials is highly desirable, providing a guideline for engineering the exciton transport performance. Notably, steady-state characterization methods cannot capture the ultrafast nonlinear diffusion process. Therefore, ultrafast optical studies on TMDs are urged to clarify the ultrafast exciton diffusion behavior.

In this work, we address the ultrafast nonlinear exciton propagation in the monolayer of TMDs with a home-built femtosecond pump-probe microscope. Highly nonlinear ultrafast exciton propagation in monolayer WSe_2 is observed at room temperature. We find that at early delay times, exciton spread extremely fast, with an equivalent diffusivity of up to 502 cm^2 s^{-1}, followed by a slow linear diffusive behavior of 20.9 cm^2 s^{-1}. The fast diffusion process is attributed to the superdiffusive behavior of the hot carriers, which are energetic. This phenomenon was further observed within $MoWSe_2$ and $MoSe_2$, with more substantial diffusivities up to 668 and 2295 cm^2 s^{-1}, respectively. Unexpected spatial shrink of exciton distribution (negative diffusion) was observed after energetic carrier superdiffusion in the $MoWSe_2$ and $MoSe_2$. Our work reveals an abnormal nonequilibrium exciton transient diffusion in monolayers WSe_2, $MoWSe_2$, and $MoSe_2$.

Materials and Methods

Sample preparation and characterization

The monolayers WSe_2, $MoWSe_2$, and $MoSe_2$ were mechanically exfoliated from the crystal (2D semiconductors) using a dry-stamping method. To suppress unwanted environmental effects from substrates, we deposited a hexagonal BN flake on the SiO_2 substrate and then transferred the monolayers onto hexagonal BN. The absorption spectra of the monolayer TMDs were carried out by a broadband halogen lamp source (Ideaoptics, HL2000-12) and an Andor spectrometer (Kymera 193i equipped with iDus CCD). For the photoluminescence (PL) measurement, a 488-nm continuous-wave laser was used to excite the sample. PL spectra were measured by an Andor spectrometer. Raman spectra were recorded on a commercial Raman spectrometer (HORIBA, LabRAM HR Evolution) with a 532-nm excitation laser. For the temperature- and excitation-dependent PL measurement, the samples are placed in the cryostat (Montana Instruments Cryostation s50).

Transient absorption microscopy

Transient absorption (TA) dynamics and spatiotemporal measurements were taken with a home-built TA microscopy (TAM) system. The schematic of the home-built TAM is shown in Fig. 1A. A Ti:sapphire femtosecond laser (Spectra-Physics, Mai Tai HP; central wavelength of 800 nm, repetition frequency of 80 MHz, pulse width of <100 fs) was used as the light source. The output beam from the Ti:sapphire laser was divided by a 70/30 beam splitter. One (70% of the output) beam was modulated by an acoustic-optic modulator (Gooch & Housego, 3080-125) at 1 MHz, which refers to a lock-in amplifier. Then, the laser wavelength of this beam was converted to 400 nm by a β-barium borate crystal for the pump. The other beam (30% of the output) was coupled to a photonic crystal fiber (SCG-800) to generate a white light supercontinuum. Then, the wavelength from the supercontinuum was selected through a narrow band-pass filter [Thorlabs; 10-nm full width at half maximum (FWHM)] for the probe. The pump and probe beams were adjusted to collinear and focused onto the sample with an objective (Olympus, MPLAPON 100× Apo, 0.95 numerical aperture). They were spatially overlapped on the sample. The transmitted beams were collected by another objective (Nikon, BD Plan 40×, 0.65 numerical aperture), and the probe was detected with an avalanche photodiode (Hamamatsu, C12702-04). The output of the avalanche photodiode was monitored with a lock-in amplifier (Zurich Instruments, HF2LI), and pump-induced changes in the probe transmission (ΔT) were obtained by demodulating at a frequency of 1 MHz. TA dynamics were acquired by stepping the delay line (Newport, DL325) at the pump path. As shown in Fig. 1B, excitons are distributed as a Gaussian function after being excited by the pump. Subsequently, the excitons continue to spread over time, and its population is still distributed as a Gaussian function. For TAM imaging, a 2-axis mirror galvanometer system (Thorlabs, GVS012) was used to scan the probe beam relative to the pump beam in space to obtain exciton diffusion profiles. Notably, all the experiments are implemented at room temperature.

Exciton diffusion model and data analysis

For quantification of exciton propagation, the TAM data are modeled with a 2D diffusion model. According to the TA measurement, the exciton diffusion in monolayer TMDs is isotropic. Therefore, the 2D diffusion can be simplified to a 1D model. The exciton population in both space and time was described by a differential equation that includes both the diffusion out of the initial volume and population decay [15], which is given by

$$\frac{\partial n(x, t)}{\partial t} = D \frac{\partial^2 n(x, t)}{\partial t^2} - \frac{n(x, t)}{\tau} \quad (1)$$

where D is the diffusion constant (diffusivity) and τ is the total exciton lifetime. Notably, the initial population $n(x, 0)$ follows the Gaussian distribution as created by a Gaussian pump beam at position (x_0) and is given by

$$n(x, 0) = N \exp \left[-\frac{(x - x_0)^2}{2\sigma_0^2} \right] \quad (2)$$

where σ_0^2 is the squared standard deviation of the Gaussian distribution. Consequently, the solution to Eq. 1 is also a Gaussian function as described by
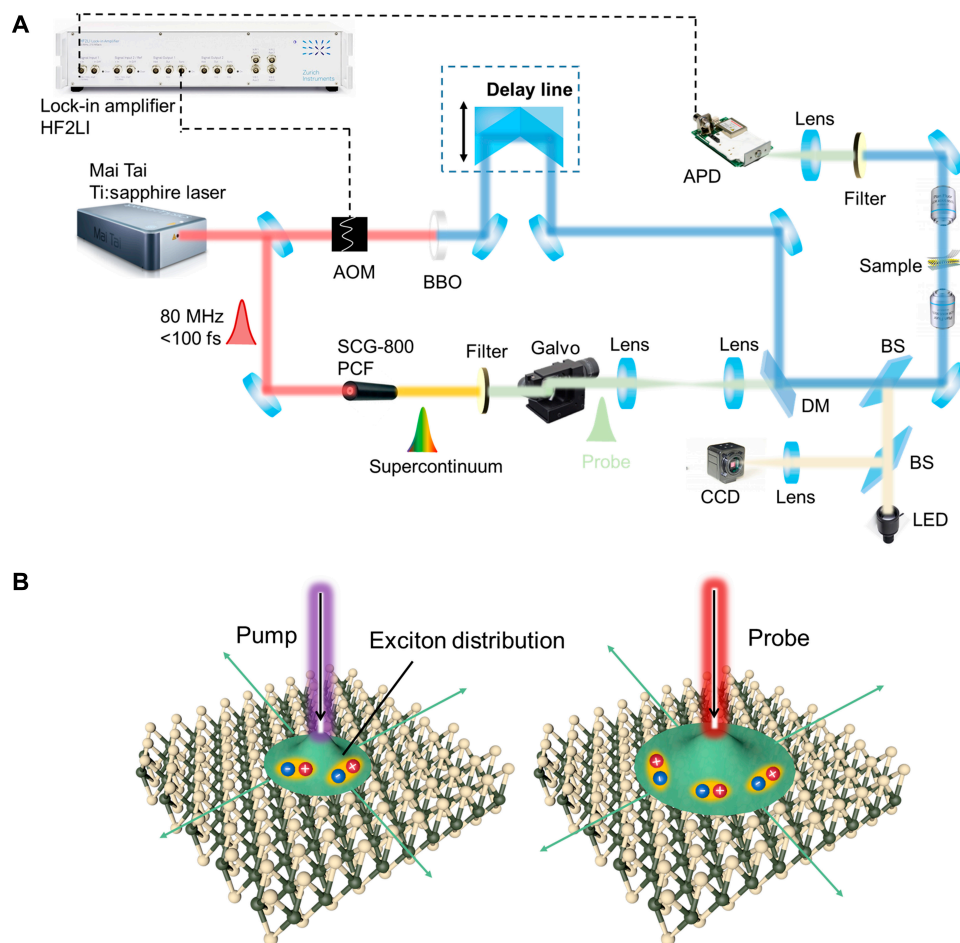
Fig. 1. Schematic diagram of TAM and photocarrier transport. (A) Schematic of a home-built TAM setup (transmission mode). (B) Schematic illustration of the exciton diffusion in monolayer TMD studied by spatially and time-resolved TAM. AOM, acoustic-optic modulator; BBO, β-barium borate; LED, light-emitting diode; DM, dichroic mirrors; BS, beam splitters.

$$n(x,t) = N\exp\left[-\frac{(x-x_0)^2}{2\sigma_t^2}\right] \quad (3)$$

The 1D TAM profiles at the various delay time in Fig. 5A to C are well fitted with the Eq. 3, and the σ_t^2 is extracted. Then, the squared standard deviation at various time σ_t^2 is plotted in Fig. 5D to F as a function of delay time.

The diffusion constant (diffusivity) D is given by

$$D = \frac{\sigma_t^2 - \sigma_0^2}{2\Delta t} \quad (4)$$

The average travel distance L can be obtained by

$$|L| = \sqrt{\sigma_t^2 - \sigma_0^2} \quad (5)$$

Results and Discussion

Optical characterization

Figure 2A presents the room-temperature optical absorption spectra of the monolayers WSe_2, $MoWSe_2$, and $MoSe_2$, showing two distinct excitonic absorptions of A exciton and B exciton. It is worth mentioning that A and B excitons are generated by the spin-orbital splitting of the valence band [42]. The B exciton absorption peak of the alloy $MoWSe_2$ (1.87 eV) is located between that of WSe_2 (2.08 eV) and $MoSe_2$ (1.78 eV). However, the A exciton absorption peaks of $MoWSe_2$ (1.57 eV) and $MoSe_2$ (1.58 eV) are almost the same, which is apparently redshifted from the WSe_2 (1.64 eV). Figure 2B shows the PL spectra collected for the 3 samples. The emission peak wavelength (~784.0 nm) of $MoWSe_2$ is still pretty close to that of $MoSe_2$ (~782.8 nm). The Raman spectra of these samples were recorded on a commercial Raman spectrometer using a 532-nm excitation laser. As shown in Fig. 2C, the expected A_{1g} mode is observed to be 260.4 cm^{-1} in WSe_2, 245.1 cm^{-1} in $MoWSe_2$, and 242.4 cm^{-1} in $MoSe_2$, respectively. The absorption, PL, and Raman spectra results show that the optical properties of the alloy $MoWSe_2$ are akin to $MoSe_2$ rather than WSe_2.

Excitation density-dependent exciton dynamics

We proceed to explore the exciton dynamics of the pristine WSe_2, $MoSe_2$, and the alloy $MoWSe_2$ at room temperature. The pump wavelength is 400 nm with an initial exciton density of 1.7×10^{13} cm^{-2}. The TA kinetic profiles of the 3 samples with the same excitation density show no substantial difference on a time scale of 100 ps, as shown in Fig. S1. In this experiment, the probe wavelength is tuned to 760 nm for WSe_2, while 780 nm
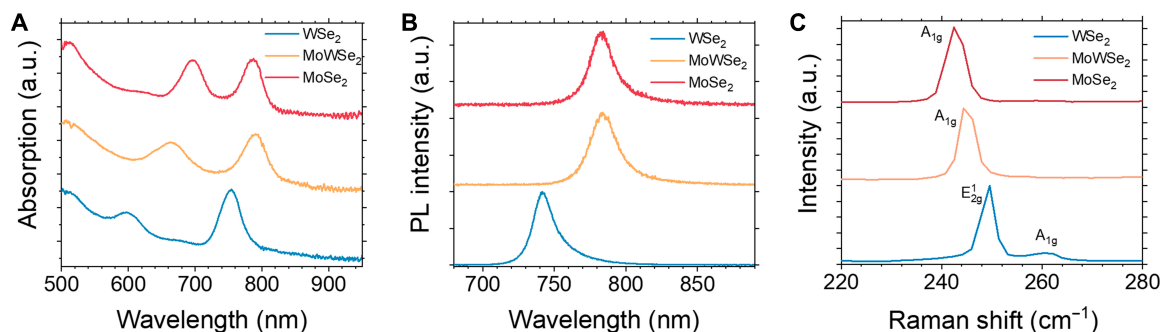
Fig. 2. Fundamental characterization of the monolayers WSe$_2$, MoWSe$_2$, and MoSe$_2$. (A) Absorption spectra of the monolayers WSe$_2$, MoWSe$_2$, and MoSe$_2$. (B) PL spectra of the monolayers WSe$_2$, MoWSe$_2$, and MoSe$_2$ excited by a 488-nm continuous-wave laser. (C) Raman spectra of the monolayers WSe$_2$, MoWSe$_2$, and MoSe$_2$. a.u., arbitrary units.
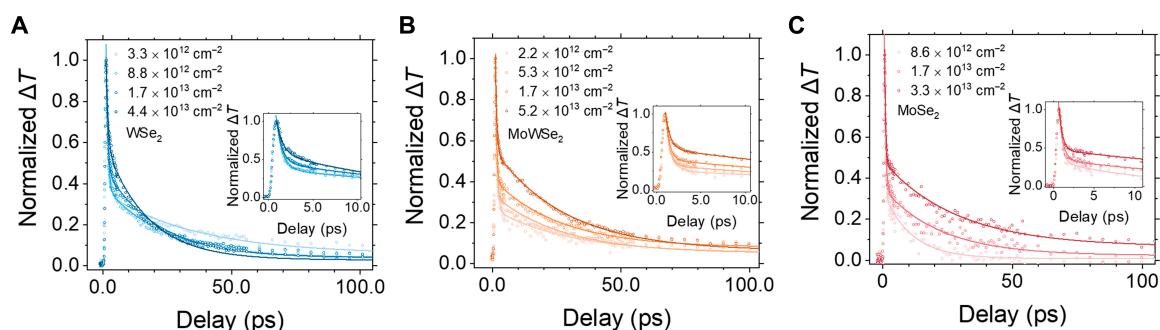

Fig. 3. Excitation density-dependent exciton dynamics. The normalized TA dynamics at different exciton densities for the monolayers (A) WSe$_2$, (B) MoWSe$_2$, and (C) MoSe$_2$. The dots are experimental results. The solid curves are triexponential fitting. The insets are the zoom of the first few picoseconds of the decays.

for MoSe$_2$ and the alloy MoWSe$_2$, referring to the A exciton resonance. The TA signal is proportional to the A exciton population. Notably, the decay of these TA signals can be well fitted by triexponential behavior, which means additional non-radiative channels are involved in addition to the intrinsic radiative recombination channel. The initial fast decay could be attributed to the nonradiative relaxation process such as defect-associated and exciton–exciton annihilation (EEA) non-radiative recombination [15,28,43].

By performing excitation density-dependent TA kinetic measurement, an anomalous TA kinetic in the 3 samples was observed. Figure 3A shows the excitation density-dependent TA dynamics of the pristine WSe$_2$ sample. Generally, the life-times tend to decrease with increasing excitation density due to the involvement of high-order recombination processes such as EEA. However, the TA dynamics in monolayer WSe$_2$ slow down at the initial 10 ps with the exciton density increase from 3.3×10^{12} to 4.4×10^{13} cm^{-2}. In addition, the following reduced lifetime after 10 ps might be explained by the relatively dominant EEA process.

To further investigate this phenomenon, we implemented the same excitation density-dependent experiment on the exfoliated monolayers MoWSe$_2$ (Fig. 3B) and MoSe$_2$ (Fig. 3C), which show the more substantial excitation-dependent dynamic behavior at the excitation density range of 10^{12} to 10^{13} cm^{-2}. The probe position-dependent experiment was also executed in MoWSe$_2$ by shifting the probe beam with respect to the pump beam. Notably, the exciton population distribution follows the Gaussian function, which means that the exciton density increases as the probe moves from the edge toward the center. As shown in Fig. S2, the lifetime increases

as the probe position moves from the outside toward the center, presenting the same dynamics as in Fig. 3B. All the dynamic curves in Fig. 3 can be well fitted by a triexponential function $n(t) = A_1 e^{-\frac{t}{\tau_1}} + A_2 e^{-\frac{t}{\tau_2}} + A_3 e^{-\frac{t}{\tau_3}}$, as shown in Fig. 3. Parameters τ_1, τ_2, and τ_3 represent the lifetime of different decay channels. The parameters A_1, A_2, and A_3, represent the proportion of exciton population recombined by the corresponding channels. To obtain a better comparison of the life-time component A_i ($i = 1, 2, 3$) of different decay channels, τ_1, τ_2, and τ_3 are fixed as constant as shown in the Table S1. The chosen fast decay lifetime is close to the time scale of trapping exciton by defects in other TMDs [43–45]. Figure S3 shows the lifetime weight of the different decay channels as a function of excitation density. For the WSe$_2$ monolayer, τ_1, τ_2, and τ_3 are attributed to defect capture, EEA, and radiative recombination, respectively. With increasing excitation density, both A_1 and A_3 decrease, while A_2 increases. For the MoWSe$_2$ and MoSe$_2$ monolayers, τ_1 and τ_2 are attributed to the defect-related recombination channel, while τ_3 is the intrinsic radiative recombination. At low-pump fluence, the short lifetime component dominates. A_1 and A_2 decrease with the increase in the excitation density, while A_3 shows the opposite tendency.

The filling of traps may account for the early anomalous TA kinetic feature. In this scenario, a portion of the excitons in the TMDs are captured by defects and relaxed by the nonradi-ative recombination channels, while the other excitons remain radiative recombination. In this context, the radiative recom-bination channel and the defect-related nonradiative channels will compete. As the density of defects in the TMDs is finite and invariant, the number of excitons captured by the defect
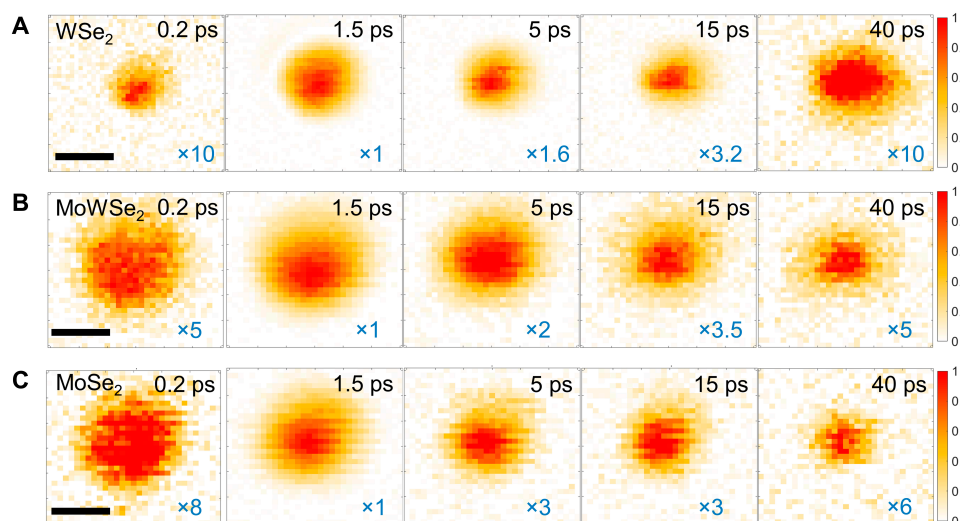
Fig. 4. Visualization of 2D spatiotemporal exciton dynamics. (A to C) 2D TAM images of the monolayers (A) WSe$_2$, (B) MoWSe$_2$, and (C) MoSe$_2$ with selected pump-probe delay times varying from 0.2 to 40 ps. The pump fluences are 1.7×10^{13} cm^{-2}. The color bar is the intensity of the differential transmission (ΔT) of the probe beam. All the figures are normalized to the maximum signal at 1.5 ps to highlight the diffusion dynamics. For clarity, every image is scaled by different factors as labeled in the figures. Scale bars, 1 μm.
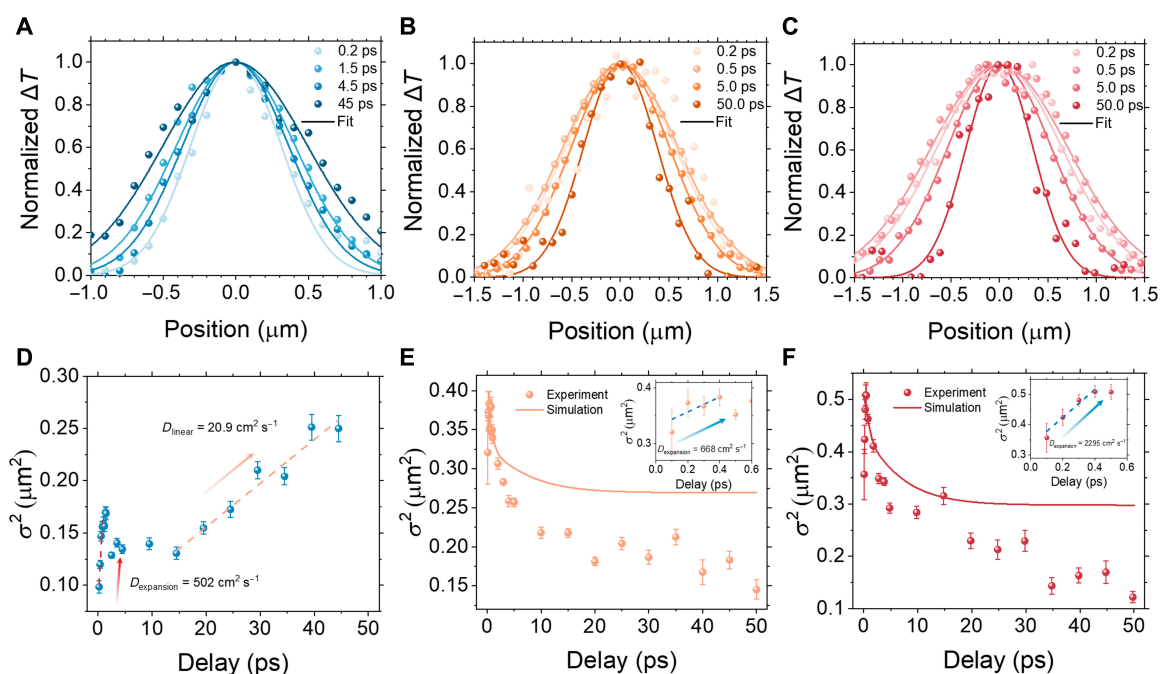

Fig. 5. Comparison of exciton diffusion in the monolayers WSe$_2$, MoWSe$_2$, and MoSe$_2$. (A to C) Normalized 1D TAM profile at various delay times for the monolayers (A) WSe$_2$, (B) MoWSe$_2$, and (C) MoSe$_2$, respectively. The TAM profiles are fitted with Gaussian functions to obtain $\sigma^2(t)$. (D to F) The evolution of squared standard deviation $\sigma^2(t)$ in the monolayers (D) WSe$_2$, (E) MoWSe$_2$, and (F) MoSe$_2$ as a function of delay time, respectively. The $\sigma^2(t)$ is fitted from the Gaussian distribution of excitons. Dots are experimental data, with error bars referring to the Gaussian fitting standard deviation. The dashed lines are linear fitting, giving the equivalent diffusion coefficient. The solid curves are simulated results by the model mentioned in Note S2. The inset is the zoom of the initial 0.6 ps, representing the hot carrier expansion process.

is limited. Consequently, more exciton will decay through the intrinsic radiative recombination channel [43], as the exciton density increase, exhibiting a longer lifetime. This is consistent with our observation. Therefore, we speculate that the slowed carrier recombination in our experiment is due to the filling of traps. To quantify the impact of defects/disorders in terms of inhomogeneous broadening, a temperature-dependent PL

experiment has been implemented as shown in Figs. S4 and S5. A detailed discussion can be found in Note S1.

Exciton-transport imaging

To investigate the transient exciton propagation behavior, we implemented ultrafast spatiotemporal measurements under a laser excitation of energy of 3.1 eV at room temperature. In the
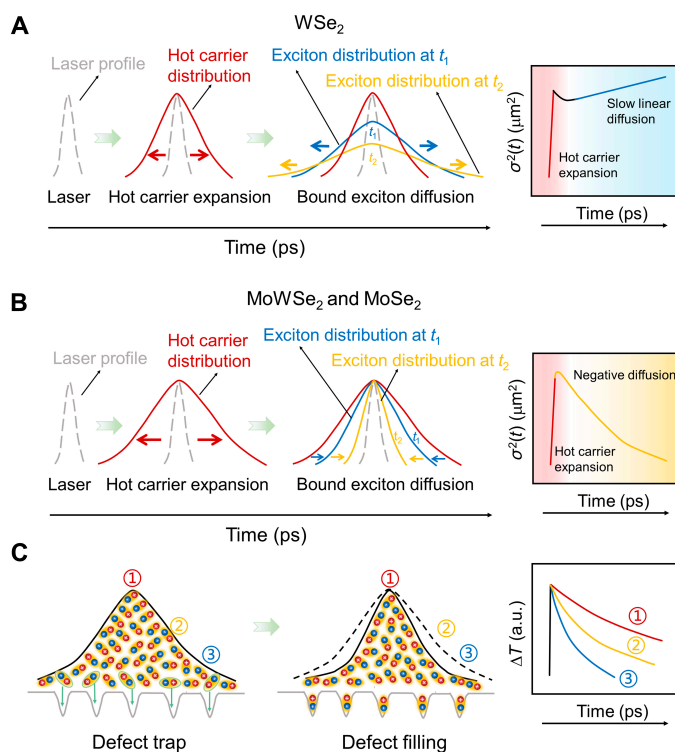
Fig. 6. Cartoon of the ultrafast spatiotemporal carrier transport in (A) WSe_2 and (B) $MoWSe_2$ and $MoSe_2$. Two distinctive processes can be observed. One is the hot carrier expansion, while the other is the bound exciton diffusion. The right panels present the diffusion patterns consistent with our experimental results. (C) Schematic illustration of the role of defect trapping in exciton transport and dynamics. The numbers ① to ③ represent the regions of different excitation densities. The corresponding exciton dynamics are shown in the right panel.

experiment, the pump beam was focused at a fixed position, while the probe beam was scanned in space. Figure 4A presents TAM images at different delay times of 0.2, 1.5, 5, 15, and 40 ps. The intensity of ΔT in 2D images is normalized to the maximum signal at 1.5 ps for comparison of the spatial distribution of exciton. In addition, every image is scaled by different factors as labeled in the figures, for clarity. At zero time delay, the initial population is generated by a Gaussian pump beam at position (x_0, y_0). The exciton profiles reflect the initial distribution of the exciton by the convolution of the pump and probe beams if no transport occurs. Exciton distribution at varied times is fitted by a Gaussian function.

At $\Delta t = 0.2$ ps, the FWHM of the exciton population distribution is close to that of the initial distribution. The spatial expansion of the A exciton distribution in the monolayer WSe_2 could be observed from $\Delta t = 0.2$ ps to $\Delta t = 1.5$ ps and subsequently seems to shrink up to $\Delta t = 15$ ps. Then the patterns present slow linear diffusion from 15 to 40 ps. Figure 4B and C shows TAM images for monolayers $MoWSe_2$ and $MoSe_2$, respectively. In both monolayers $MoWSe_2$ and $MoSe_2$, the FWHM of the exciton profiles at $\Delta t = 0.2$ ps are substantially larger than that in monolayer WSe_2, as shown in Fig. 4A. The reason might be the effective hot carrier expansion that cannot be resolved by our instrument because of its intrinsic limitation of temporal resolution. Subsequently, the exciton distribution exhibit negative diffusion behavior.

To reduce the data redundancy and quantitatively describe such an expansion process, we implement the 1D exciton profiles scanning at different delay times ranging from 0.2 to 50 ps.

Figure 5A to C displays the normalized 1D TAM profile at various delay time for the monolayers WSe_2, $MoWSe_2$, and $MoSe_2$, respectively. All profiles can be well described by the Gaussian function, and we extract the parameter $\sigma^2(t)$ for analysis (see details in Materials and Methods). Figure 5D to F presents the high-resolution temporal evolution of the extracted squared standard deviation $\sigma^2(t)$ from the Gaussian distribution within 50-ps pump-probe delay time in the exfoliated monolayers WSe_2, $MoWSe_2$, and $MoSe_2$, respectively. Notably, the exciton diffusion behavior in Fig. 5D to F is consistent with that in Fig. 4. Ultrafast hot-carrier expansion is observed in the initial time for all 3 samples, presenting an equivalent diffusivity of 502, 668, and 2295 $cm^2 s^{-1}$, respectively. Compare to WSe_2, $MoSe_2$ and $MoWSe_2$ present stronger hot-carrier expansion process [the maximum $\sigma^2(t)$ for WSe_2, $MoSe_2$, and $MoWSe_2$ are 0.17, 0.51, and 0.38 μm^2, respectively]. After that, a small contraction ($L = -200$ nm) followed by a slow linear diffusive behavior ($D = 20.9$ $cm^2 s^{-1}$) is observed in WSe_2, as shown in Fig. 5D. This anomalous diffusion process was previously reported in layered WS_2 [32], which is attributed to the involvement of both hot carrier-dominated expansion and exciton-limited diffusion.

In contrast, the monolayers $MoSe_2$ and $MoWSe_2$ exhibit negative diffusion behavior after 0.5 ps (Fig. 5E and F). The ultrafast exciton-transport imaging results reveal the transient superdiffusion in 3 different TMD materials. The equivalent diffusivity of this superdiffusive behavior is 10^2 to 10^3 $cm^2 s^{-1}$, breaking the limit of the slow linear diffusion. At times longer than 50 ps, there is adequate evidence to believe that the excitons in monolayer WSe_2 would continue slow linear diffusion as reported by many other works [15,28,30,46] since the results present a clear trend of linear diffusion behavior ranging from 15 to 50 ps. Considering the weak diffusion capability in the monolayers $MoWSe_2$ and $MoSe_2$, exciton population distribution would further shrink after 50 ps until it approaches the initial distribution at zero delay time (i.e., the convolution of the pump and probe beam).

Recent research reported enhanced neutral exciton diffusion in monolayer WS_2 by EEA. As the generation rate increase from 10^{14} to 10^{20} cm^{-2}, the effective diffusion coefficient increase from 1 to 100 $cm^2 s^{-1}$ [47]. However, this mechanism is unable to explain our results. First and foremost, the rapid expansion occurs within about 1 ps, when the hot carriers still dominate and high concentrations of bound excitons have not yet been established through thermalization and cooling. Second, if the EEA is dominant, then the exciton lifetimes are expected to decrease with increasing excitation density, which is inconsistent with our TA dynamics in Fig. 3. Third, the EEA is an exciton interaction that occurs after a high exciton concentration builds up. Therefore, the time for the EEA should be persistent for at least tens of picoseconds according to the nonsingle exponential regime [48,49], while it is not in our case.

The underlying physical process for the observed abnormal transient diffusion could be complex. Figure 6 provides a cartoon diagram illustrating the ultrafast spatiotemporal carrier transport in WSe_2, $MoSe_2$, and $MoWSe_2$. The entire diffusion process can be divided into two parts. One part is the transient superdiffusion within 1 ps due to the hot carrier-dominated expansion, and the other is the slow linear or negative diffusion due to the exciton-limited diffusion. For the transient superdiffusive behavior, nonthermal equilibrium photogenerated carriers are generated in the monolayer TMDs under the excitation

of the high-energy photon. These photogenerated carriers then experience an ultrafast thermalization process within tens of femtoseconds due to the carrier–carrier scattering [50]. At this moment, the hot carriers are energetic with excess kinetic energy [51]. Meanwhile, the hot carrier will experience rapid expansion and long-length transport driven by the carrier temperature-induced pressure gradient [34], which is distinct from the classical population gradient-induced transport. Subsequently, the excess energy of the hot carriers is transferred to the lattice via carrier–phonon scattering on a time scale of $\approx$1 ps, accompanied by the formation of bound excitons. Therefore, we can observe an initial rapid expansion by probing the exciton population as the previously propagated hot carriers are converted into bound excitons.

It is noteworthy that the excess kinetic energy in Mo-riched samples is more than that in W-riched samples due to their bandgap differences. Excess kinetic energy is the driving force for expansion. Hence, the one possessing more excess kinetics energy may propagate faster [36]. It explains that the equivalent diffusivity of MoWSe$_2$ (668 cm^2 s^{-1}) and MoSe$_2$ (2295 cm^2 s^{-1}) is larger than that of WSe$_2$ (502 cm^2 s^{-1}). Rosati et al. [52] observed a transient diffusion coefficient of up to 50 cm^2 s^{-1} in the first picoseconds after resonant excitation, where the WSe$_2$ monolayer is cooled down to cryogenic temperatures. Notably, there is no carrier contributions expected because of resonant excitation. The transient diffusion coefficient in our experiments is an order of magnitude larger than reported in the literature [52]. This substantial difference fully illustrates the key role played by hot carriers in superdiffusion and its prospect of breaking the limit of conventional slow diffusion of excitons.

Next, we discuss the physical process of slow linear diffusion (WSe$_2$) and negative diffusion (MoWSe$_2$ and MoSe$_2$). For the monolayer WSe$_2$, classical bound exciton diffusion is responsible for the slow linear diffusive behavior. While the reported diffusion coefficient varies greatly, with values from a few square centimeters per second to 15 ± 5 cm^2 s^{-1} in the monolayer WSe$_2$. The discrepancy could be due to the material's quality or different experimental conditions. For the monolayers MoWSe$_2$ and MoSe$_2$, we consider that negative diffusion does not occur in real space but is related to exciton decay at different positions in space. The dynamic results in Fig. 3B and C demonstrate that the higher exciton density leads to a longer lifetime due to the filling of the defect (also see Fig. 6C). Therefore, the slower decay rate leaves more excitons in the center. Then, the exciton profiles seem to shrink as a function of delay time. Compared to the monolayer WSe$_2$, the exciton diffusion length of MoSe$_2$ is much shorter, as shown in Fig. S6. As shown in Fig. 5E and F, the $\sigma^2(t)$ gradually decreases and approaches the convolution of the pump and probe beam (0.12 μm^2) with increasing delay time, indicating that there is almost no real-space diffusion in both MoWSe$_2$ and MoSe$_2$. Our ultrafast spatiotemporal imaging shows consistent results with steady-state diffusion.

To verify the mechanism, we performed a simulation of the exciton distribution at various times (Fig. S7 and see the detail of the modeling and simulation in Note S2). The simulated σ^2 as a function of delay time for monolayers MoWSe$_2$ and MoSe$_2$ shows the same trend as the experimental results (Fig. 5E and F). The temperature is reported as an important factor that affects diffusion [52,53]. We emphasize that the transient diffusion in the first picosecond should be dominated by the nonthermal equilibrium hot carrier. Hence, the carrier temperature rather than the lattice temperature should be considered.

With higher carrier temperature, the hot carrier expansion is expected to be enhanced [32] because of the higher kinetic energy. Thus, the "hot carrier" shows high discrepancy from the "cold carriers" in diffusion and optical properties (see more discussion in Note S3).

Exciton density is also important in diffusion behavior. For the transient superdiffusion, carrier temperature would increase to up to thousands of kelvin with the increasing excitation power [38]. Higher carrier temperature brings a giant temperature gradient, leading to faster hot carrier expansion as reported in multilayer WS$_2$ by Liu et al. [32]. For the slow linear diffusion, the rest excitons are protected from the defects due to the filling of defects with increased excitation power, leading to increased exciton diffusion. In addition, other effects, such as Auger recombination and the Seebeck effect, may occur at higher excitation densities, which may further enhance the actual/effective diffusion. Kulig et al. [30] reported a substantial increase in the effective diffusion coefficient of monolayer WS$_2$ over two orders of magnitude due to the interplay of exciton interactions and diffusion accounting for Auger recombination. By introducing a thermal drift into the diffusion equation, the substantial increase in the diffusion coefficient can be well explained, considering more efficient thermal currents with increasing excitation density [31]. Cordovilla Leon et al. [54] observed saturation of the hot exciton gas' expansion rate at high excitation densities due to the balance between Auger-assisted hot exciton generation and the phonon-assisted hot exciton relaxation processes. At higher excitation power, excitons would experience a stronger excitonic drift force driven by the repulsive dipolar interaction, enhancing the diffusion coefficient by one order of magnitude [55]. In our case, the pump fluence is on the order of 10^{13} cm^{-2}. Therefore, we expect an increase in the effective diffusion coefficient in monolayer WSe$_2$ at higher exciton densities. As for the monolayers MoWSe$_2$ and MoSe$_2$ (see detailed discussion in Note S4), we expect that the negative diffusion will slow down with increasing excitation density.

Conclusion

In summary, we have investigated the nonequilibrium exciton transient superdiffusive behavior in monolayers WSe$_2$, MoWSe$_2$, and MoSe$_2$ with a home-built pump-probe microscope. The exciton density-dependent dynamics and ultrafast spatiotemporal imaging experiment are implemented. Hot carrier-dominated fast expansion was observed at the early delay time for all 3 samples. The equivalent diffusivity for monolayers WSe$_2$, MoWSe$_2$, and MoSe$_2$ is 502, 668, and 2295 cm^2 s^{-1}, respectively. For monolayer WSe$_2$, we observe a small contraction followed by a slow linear diffusive behavior ($D = 20.9$ cm^2 s^{-1}) at a later time, which can be explained by the involvement of both hot carrier-dominated expansion and exciton-limited diffusion. In contrast, an unexpected negative exciton diffusion behavior was observed in monolayers MoWSe$_2$ and MoSe$_2$. In combination with the results of excitation density-dependent experiments, this phenomenon is attributed to be related to exciton decay at different positions in space rather than occurring in real space. The ultrafast exciton-transport imaging results demonstrate the transient superdiffusion in 3 different TMD materials. The experimentally observed unusual behavior in the exciton diffusion highlights 2D materials as a particularly promising platform for excitonic physics. The results should be relevant to excitonic and photonic applications, stimulating further research.

Acknowledgments

Data Availability

The data that support the findings of this study are available from the corresponding authors upon reasonable request.

Supplementary Materials

Fig. S1. Comparison of exciton dynamics between the monolayers WSe_2, $MoWSe_2$, and $MoSe_2$.
Fig. S2. The normalized TA dynamics probed at different positions for the monolayer $MoWSe_2$.
Fig. S3. The fitted lifetime weight in Fig. 3 is a function of excitation density for monolayers (A) WSe_2, (B) $MoWSe_2$, and (C) $MoSe_2$.
Fig. S4. Normalized PL of monolayers (A) WSe_2, (B) $MoWSe_2$, and (C) $MoSe_2$ at different temperatures.
Fig. S5. Temperature broadening of the neutral A exciton linewidth for 3 different TMD monolayers.
Fig. S6. Comparison of steady-state diffusion between monolayers WSe_2 and $MoSe_2$.
Fig. S7. Simulated exciton distribution at various times for monolayers $MoWSe_2$ and $MoSe_2$.
Fig. S8. Normalized PL of monolayers (A) WSe_2, (B) $MoWSe_2$, and (C) $MoSe_2$ at 15 K with different excitation densities.
Fig. S9. Linewidth of the neutral A exciton fitted from the PL in Fig. S8 versus exciton density for 3 different monolayers.
Table S1. Fixed fitting parameters of all 3 TMD monolayers for Fig. S3.
Note S1. Quantitative analysis of the impact of defects in terms of inhomogeneous broadening.
Note S2. Model and simulation of the defect-related anomalous exciton diffusion.
Note S3. The role of temperature in slow diffusion, linewidth, and decay.
Note S4. The role of excitation density in negative diffusion and linewidth.

References

1. Manzeli S, Ovchinnikov D, Pasquier D, Yazyev OV, Kis A. 2D transition metal dichalcogenides. *Nat Rev Mater*. 2017;2(8): Article 17033.
2. Liu X, Hu J, Yue C, Della Fera N, Ling Y, Mao Z, Wei J. High performance field-effect transistor based on multilayer tungsten disulfide. *ACS Nano*. 2014;8(10):10396–10402.
3. Tsai ML, Su SH, Chang JK, Tsai DS, Chen CH, Wu CI, Li LJ, Chen LJ, He JH. Monolayer MoS_2 heterojunction solar cells. *ACS Nano*. 2014;8(8):8317–8322.
4. Hwangbo S, Hu L, Hoang AT, Choi JY, Ahn JH. Wafer-scale monolithic integration of full-colour micro-LED display using MoS_2 transistor. *Nat Nanotechnol*. 2022;17(5):500–506
5. Dasgupta A, Gao J, Yang X. Atomically thin nonlinear transition metal dichalcogenide holograms. *Nano Lett*. 2019;19(9):6511–6516.4
6. Splendiani A, Sun L, Zhang Y, Li T, Kim J, Chim CY, Galli G, Wang F. Emerging photoluminescence in monolayer MoS_2. *Nano Lett*. 2010;10(4):1271–1275.
7. Mak KF, Lee C, Hone J, Shan J, Heinz TF. Atomically thin MoS_2: A new direct-gap semiconductor. *Phys Rev Lett*. 2010;105(13):Article 136805.
8. Xiao D, Liu GB, Feng W, Xu X, Yao W. Coupled spin and valley physics in monolayers of MoS_2 and other group-VI dichalcogenides. *Phys Rev Lett*. 2012;108(19):Article 196802.
9. Unuchek D, Ciarrocchi A, Avsar A, Sun Z, Watanabe K, Taniguchi T, Kis A. Valley-polarized exciton currents in a van der Waals heterostructure. *Nat Nanotechnol*. 2019;14(12):1104–1109.
10. Ugeda MM, Bradley AJ, Shi SF, da Jornada FH, Zhang Y, Qiu DY, Ruan W, Mo SK, Hussain Z, Shen ZX, et al. Giant bandgap renormalization and excitonic effects in a monolayer transition metal dichalcogenide semiconductor. *Nat Mater*. 2014;13(12):1091–1095.
11. Ross JS, Wu S, Yu H, Ghimire NJ, Jones AM, Aivazian G, Yan J, Mandrus DG, Xiao D, Yao W, et al. Electrical control of neutral and charged excitons in a monolayer semiconductor. *Nat Commun*. 2013;4:1474.
12. Busschaert S, Reimann R, Cavigelli M, Khelifa R, Jain A, Novotny L. Transition metal dichalcogenide resonators for second harmonic signal enhancement. *ACS Photonics* 2020;7(9):2482–2488.
13. Kumar N, Najmaei S, Cui Q, Ceballos Q, Ajayan PM, Lou J, Zhao H. Second harmonic microscopy of monolayer MoS_2. *Phys Rev B*. 2013;87:Article 161403.
14. Cadiz F, Robert C, Courtade E, Manca M, Martinelli L, Taniguchi T, Watanabe K, Amand T, Rowe ACH, Paget D, et al. Exciton diffusion in WSe_2 monolayers embedded in a van der Waals heterostructure. *Appl Phys Lett*. 2018;112:Article 152106.
15. Yuan L, Wang T, Zhu T, Zhou M, Huang L. Exciton dynamics, transport, and annihilation in atomically thin two-dimensional semiconductors. *J Phys Chem Lett*. 2017;8(14):3371–3379.
16. Mouri S, Miyauchi Y, Toh M, Zhao W, Eda G, Matsuda K. Nonlinear photoluminescence in atomically thin layered WSe_2 arising from diffusion-assisted exciton-exciton annihilation. *Phys Rev B*. 2014;90(15):Article 155449.
17. Uddin SZ, Kim H, Lorenzon M, Yeh M, Lien DH, Barnard ES, Htoon H, Weber-Bargioni A, Javey A. Neutral exciton diffusion in monolayer MoS_2. *ACS Nano*. 2020;14(10):13433–13440.
18. Jauregui LA, Joe AY, Pistunova K, Wild DS, High AA, Zhou Y, Scuri G, De Greve K, Sushko A, Yu CH, et al. Electrical control of interlayer exciton dynamics in atomically thin heterostructures. *Science*. 2019;366(6467):870–875.
19. Yuan L, Zheng B, Kunstmann J, Brumme T, Kuc AB, Ma C, Deng S, Blach D, Pan A, Huang L. Twist-angle-dependent interlayer exciton diffusion in WS_2-WSe_2 heterobilayers. *Nat Mater*. 2020;19(6):617–623.
20. Datta K, Lyu Z, Li Z, Taniguchi T, Watanabe K, Deotare PB. Spatiotemporally controlled room-temperature

exciton transport under dynamic strain. *Nat Photonics*. 2022;16(3):242–247.

21. Vögele XP, Schuh D, Wegscheider W, Kotthaus JP, Holleitner AW. Density enhanced diffusion of dipolar excitons within a one-dimensional channel. *Phys Rev Lett*. 2009;103(12):Article 126402.

22. Rosati R, Perea-Causín R, Brem S, Malic E. Negative effective excitonic diffusion in monolayer transition metal dichalcogenides. *Nanoscale*. 2020;12(1):356–363.

23. Peng R, Ripin A, Ye Y, Zhu J, Wu C, Lee S, Li H, Taniguchi T, Watanabe K, Cao T, et al. Long-range transport of 2D excitons with acoustic waves. *Nat Commun*. 2022;13(1):1334.

24. Unuchek D, Ciarrocchi A, Avsar A, Watanabe K, Taniguchi T, Kis A. Room-temperature electrical control of exciton flux in a van der Waals heterostructure. *Nature*. 2018;560(7718):340–344.

25. Ciarrocchi A, Tagarelli F, Avsar A, Kis A. Excitonic devices with van der Waals heterostructures: Valleytronics meets twistronics. *Nat Rev Mater*. 2022;7(6):449–464.

26. Qi P, Dai Y, Luo Y, Tao G, Zheng L, Liu D, Zhang T, Zhou J, Shen B, Lin F, et al. Giant excitonic upconverted emission from two-dimensional semiconductor in doubly resonant plasmonic nanocavity. *Light Sci Appl*. 2022;11(1):176.

27. Kumar N, Cui Q, Ceballos F, He D, Wang Y, Zhao H. Exciton diffusion in monolayer and bulk $MoSe_2$. *Nanoscale*. 2014;6(9):4915–4919.

28. Liu H, Wang C, Zuo Z, Liu D, Luo J. Direct Visualization of exciton transport in defective few-layer WS_2 by ultrafast microscopy. *Adv Mater*. 2020;32(2):Article e1906540.

29. Li Z, Lu X, Cordovilla Leon DF, Lyu Z, Xie H, Hou J, Lu Y, Guo X, Kaczmarek A, Taniguchi T, et al. Interlayer exciton transport in $MoSe_2/WSe_2$ heterostructures. *ACS Nano*. 2021;15(1):1539–1547.

30. Kulig M, Zipfel J, Nagler P, Blanter S, Schüller C, Korn T, Paradiso N, Glazov MM, Chernikov A. Exciton diffusion and halo effects in monolayer semiconductors. *Phys Rev Lett*. 2018;120(20):Article 207401.

31. Perea-Causín R, Brem S, Rosati R, Jago R, Kulig M, Ziegler JD, Zipfel J, Chernikov A, Malic E. Exciton propagation and halo formation in two-dimensional materials. *Nano Lett*. 2019;19(10):7317–7323.

32. Liu Q, Wei K, Tang Y, Xu Z, Cheng X, Jiang T. Visualizing hot-carrier expansion and cascaded transport in ws2 by ultrafast transient absorption microscopy. *Adv Sci (Weinh)*. 2022;9(10):Article e2105746.

33. Klas R, Kirsche A, Gebhardt M, Buldt J, Stark H, Hädrich S, Rothhardt J, Limpert J. Ultra-short-pulse high-average-power megahertz-repetition-rate coherent extreme-ultraviolet light source. *PhotoniX*. 2021;2(1):Article 4.

34. Najafi E, Ivanov V, Zewail A, Bernardi M. Super-diffusion of excited carriers in semiconductors. *Nat Commun*. 2017;8:Article 15177.

35. Berghuis AM, Raziman TV, Halpin A, Wang S, Curto AG, Rivas JG. Effective negative diffusion of singlet excitons in organic semiconductors. *J Phys Chem Lett*. 2021;12(4):1360–1366.

36. Guo Z, Wan Y, Yang M, Snaider J, Zhu K, Huang L. Long-range hot-carrier transport in hybrid perovskites visualized by ultrafast microscopy. *Science*. 2017;356(6333):59–62.

37. Sung J, Schnedermann C, Ni L, Sadhanala A, Chen RYS, Cho C, Priest L, Lim JM, Kim H-K, Monserrat B, et al. Long-range ballistic propagation of carriers in methylammonium lead iodide perovskite thin films. *Nat Phys*. 2019;16(2):171–176.

38. Block A, Liebel M, Yu R, Spector M, Sivan Y, García de Abajo FJ, van Hulst NF. Tracking ultrafast hot-electron diffusion in space and time by ultrafast thermomodulation microscopy. *Sci Adv*. 2019;5(5):Article eaav8965.

39. Segovia M, Xu X. High accuracy ultrafast spatiotemporal pump-probe measurement of electrical thermal transport in thin film gold. *Nano Lett*. 2021;21(17):7228–7235.

40. Rawat A, Jena N, Dimple D, De Sarkar A. A comprehensive study on carrier mobility and artificial photosynthetic properties in group VI B transition metal dichalcogenide monolayers. *J Mater Chem A.*. 2018;6(18):8693–8704.

41. Li X, Lin M-W, Basile L, Hus SM, Puretzky AA, Lee J, Kuo Y-C, Chang L-Y, Wang K, Idrobo JC, et al. Isoelectronic tungsten doping in monolayer $MoSe_2$ for carrier type modulation. *Adv Mater*. 2016;28(37):8240–8247.

42. Zhao W, Ghorannevis Z, Chu L, Toh M, Kloc C, Tan P-H, Eda G. Evolution of electronic structure in atomically thin sheets of WS_2 and WSe_2. *ACS Nano*. 2013;7(1):791–797.

43. Li Z, Zeng Y, Ou Z, Zhang T, Du R, Wu K, Guo Q, Jiang W, Xu Y, Li T, et al. Defects inducing anomalous exciton kinetics in monolayer WS_2. *Nano Res*. 2021;15(2):1616–1622.

44. Shi H, Yan R, Bertolazzi S, Brivio J, Gao B, Kis A, Jena D, Xing HG, Huang L. Exciton dynamics in suspended monolayer and few-layer MoS_2 2D crystals. *ACS Nano* 2013;7(2):1072–1080.

45. Chen K, Ghosh R, Meng X, Roy A, Kim J-S, He F, Mason SC, Xu X, Lin J-F, Akinwande D, et al. Experimental evidence of exciton capture by mid-gap defects in CVD grown monolayer $MoSe_2$. *npj 2D Mater Appl*. 2017;1(1):15.

46. Cui Q, Ceballos F, Kumar N, Zhao H. Transient absorption microscopy of monolayer and bulk WSe_2. *ACS Nano* 2014;8(3):2970–2976.

47. Uddin SZ, Higashitarumizu N, Kim H, Yi J, Zhang X, Chrzan D, Javey A. Enhanced neutral exciton diffusion in monolayer WS_2 by exciton-exciton annihilation. *ACS Nano* 2022;16(5):8005–8011.

48. Kumar N, Cui Q, Ceballos F, He D, Wang Y, Zhao H. Exciton-exciton annihilation in $MoSe_2$ monolayers. *Phys Rev B*. 2014;89:Article 125427.

49. Liu H, Wang C, Liu D, Luo J. Neutral and defect-induced exciton annihilation in defective monolayer WS_2. *Nanoscale*. 2019;11(16):7913–7920.

50. Trovatello C, Katsch F, Borys NJ, Selig M, Yao K, Borrego-Varillas R, Scotognella F, Kriegel I, Yan A, Zettl A, et al. The ultrafast onset of exciton formation in 2D semiconductors. *Nat Commun*. 2020;11(1):5277.

51. Li Y, Liu W, Wang Y, Xue Z, Leng YC, Hu A, Yang H, Tan PH, Liu Y, Misawa H. Ultrafast electron cooling and decay in monolayer WS_2 revealed by time- and energy-resolved photoemission electron microscopy. *Nano Lett* 2020;20(5):3747–3753.

52. Rosati R, Wagner K, Brem S, Perea-Causin R, Ziegler JD, Zipfel J, Taniguchi T, Watanabe K, Chernikov A, Malic E. Non-equilibrium diffusion of dark excitons in atomically thin semiconductors. *Nanoscale*. 2021;13:19966–19972.

53. Wagner K, Zipfel J, Rosati R, Wietek E, Ziegler JD, Brem S, Perea-Causín R, Taniguchi T, Watanabe K, Glazov MM, et al. Nonclassical exciton diffusion in monolayer WSe_2. *Phys Rev Lett*. 2021;127(7):Article 076801.

54. Cordovilla Leon DF, Li Z, Jang SW, Deotare PB. Hot exciton transport in WSe$_2$ monolayers. *Phys Rev B*. 2019;100:Article 241401.

55. Sun Z, Ciarrocchi A, Tagarelli F, Marin JFG, Watanabe K, Taniguchi T, Kis A. Excitonic transport driven by repulsive dipolar interaction in a van der Waals heterostructure. *Nat Photonics*. 2022;16(1):79–85.

56. Ajayi OA, Ardelean JV, Shepard GD, Wang J, Antony A, Taniguchi T, Watanabe K, Heinz TF, Strauf S, Zhu XY, et al. Approaching the intrinsic photoluminescence linewidth in transition metal dichalcogenide monolayers. *2D Mater*. 2017;4(3):Article 031011.

57. Raja A, Waldecker L, Zipfel J, Cho Y, Brem S, Ziegler JD, Kulig M, Taniguchi T, Watanabe K, Malic E, et al. Dielectric disorder in two-dimensional materials. *Nat Nanotechnol*. 2019;14(9):832–837.

58. Cadiz F, Courtade E, Robert C, Wang G, Shen Y, Cai H, Taniguchi T, Watanabe K, Carrere H, Lagarde D, et al. Excitonic linewidth approaching the homogeneous limit in MoS$_2$-based van der Waals heterostructures. *Phys Rev X*. 2017;7(12):Article 021026.

59. You Y, Zhang X-X, Berkelbach TC, Hybertsen MS, Reichman DR, Heinz TF. Observation of biexcitons in monolayer WSe$_2$. *Nat Phys*. 2015;11(6):477–481.

60. Selig M, Berghäuser G, Raja A, Nagler P, Schuller C, Heinz TF, Korn T, Chernikov A, Malic E, Knorr A. Excitonic linewidth and coherence lifetime in monolayer transition metal dichalcogenides. *Nat Commun*. 2016;7(1):13279.

61. Dey P, Paul J, Wang Z, Stevens CE, Liu C, Romero AH, Shan J, Hilton DJ, Karaiskaj D. *Phys Rev Lett*. 2016;116(12):Article 127402.

62. Robert C, Lagarde D, Cadiz F, Wang G, Lassagne B, Amand T, Balocchi A, Renucci P, Tongay S, Urbaszek B, Marie X. Exciton radiative lifetime in transition metal dichalcogenide monolayers. *Phys Rev B*. 2016;93(20):Article 205423.

63. Zhang XX, You Y, Zhao SY, Heinz TF. Experimental evidence for dark excitons in monolayer WSe$_2$. *Phys Rev Lett* 2015;115(25):Article 257403.

64. Li X-Z, Aihemaiti N, Fang H-H, Huang G-Y, Zhou Y-K, Wang X-J, Zhang Y, Xing R, Peng S, Bai B, et al. Optical visualization of photoexcitation diffusion in all-inorganic perovskite at high temperature. *J Phys Chem Lett*. 2022;13(33):7645–7652.

65. Moody G, Kavir Dass C, Hao K, Chen CH, Li LJ, Singh A, Tran K, Clark G, Xu X, Berghäuser G, et al. Intrinsic homogeneous linewidth and broadening mechanisms of excitons in monolayer transition metal dichalcogenides. *Nat Commun*. 2015;6:8315.